Suspension properties at finite Reynolds number from simulated shear flow

2 authors:

Pandurang Kulkarni
Statoil, Houston
17 PUBLICATIONS   **551** CITATIONS

SEE PROFILE

Jeffrey F Morris
City College of New York
239 PUBLICATIONS   **11,433** CITATIONS

SEE PROFILE

Suspension properties at finite Reynolds number from simulated shear flow

Pandurang M. Kulkarni and Jeffrey F. Morris[a)]

Levich Institute and Department of Chemical Engineering, City College of the City University of New York, New York, New York 10031, USA

This work examines the role of particle-scale inertia in a monodisperse suspension of non-Brownian and neutrally buoyant spherical particles subjected to simple-shear flow. The dimensionless parameters governing the problem are the solid-volume fraction ϕ and the Reynolds number defined $\mathrm{Re} = \rho \dot{\gamma} a^2 / \mu$, where a is the sphere radius, $\dot{\gamma}$ is the shear rate, and μ and ρ are the viscosity and density of the fluid, respectively. Using numerical simulations in a wall-bounded domain via the lattice-Boltzmann method, the bulk rheological properties of relative viscosity, normal stress differences, and particle pressure are reported for $0.01 \leq \mathrm{Re} < 5$ and $0.05 \leq \phi \leq 0.3$. The anisotropy in microstructure at finite Re is studied through the pair distribution function $g(\mathbf{r})$. Also presented are the probability density functions of particle velocity fluctuations in gradient and vorticity directions. Comparisons to low Reynolds number theory and simulations are provided wherever possible. © *2008 American Institute of Physics*. [DOI: 10.1063/1.2911017]

I. INTRODUCTION

The rheological properties of suspensions are important in design of operations in many fields of industry, e.g., suspension coating and slurry transport. Much progress has been made toward understanding viscous suspensions at low particle Reynolds numbers. Under dilute conditions, hydrodynamic interactions between the particles can be neglected and the suspension exhibits Newtonian rheology, with a relative viscosity $\mu_r = \mu_s / \mu = 1 + 2.5\phi$, where μ_s is the effective viscosity of the suspension and μ is the viscosity of the suspending fluid.[1] Deviations from Newtonian behavior are observed at higher ϕ. Experimental findings show the presence of normal stresses exhibited by viscous suspensions at low Reynolds numbers,[2–4] as well as shear thickening.[5] These experiments were primarily carried out for concentrated suspensions ($\phi \gtrsim 0.3$) where the normal stresses become large enough for reliable measurement. The isotropic particle stress, termed the particle pressure (Π), was disregarded in earlier studies,[1,6] but has been reported in a recent study.[3]

Computer simulations have significantly improved our understanding of viscous suspensions. Brady and co-workers[7,8] have developed the Stokesian Dynamics, a method for simulating suspensions at low Reynolds number which can accurately capture many-body hydrodynamic interactions. An important issue which simulation has probed is that of particle microstructure in flow, an issue experimentally considered by Parsi and Gadala-Maria.[9] Simulation studies have explored the structural asymmetry[10] and related this to the shear-induced normal stresses.[11–13] Simulations of Sierou and Brady[13] by Stokesian Dynamics showed that both first (N_1) and second (N_2) normal stress differences are negative for $0.1 \leq \phi \leq 0.5$, with $N_1 \approx N_2$ and increasing in magnitude with the concentration. They found generally good qualitative agreement for N_1, N_2, and Π with experimental results of Zarraga *et al.*[3] and Singh and Nott,[4] with Π inferred rather than directly measured experimentally, although the experiments show $|N_2|/|N_1|$ to be larger than found in simulation. Issues related to the normal stresses in concentrated suspensions include particle migration in curvilinear[14] and pressure-driven flows.[15,16]

Our understanding of Stokes-flow suspensions is much more advanced than that of suspensions with finite inertia at the particle scale, implying nonzero $\mathrm{Re} = \rho \dot{\gamma} a^2 / \mu$, where a is the radius of a spherical particle, $\dot{\gamma}$ is the shear rate, and ρ is the fluid density. In the dilute limit, simple-shear flow with finite inertia over a sphere was analyzed using matched asymptotic expansions for $\mathrm{Re} \ll 1$; weak inertia was found to cause an increase in the particle contribution to the viscosity of $O(\mathrm{Re}^{3/2})$ and by breaking the symmetry of Stokes flow to give rise to $O(\mathrm{Re})$ normal stresses.[17] Full solution of the Navier–Stokes equations for finite-Reynolds-number flow in suspensions of mobile particles is challenging. Conventional computational fluid dynamical techniques such as the finite element method (FEM) allow the refinement of grids near the particle surfaces and have largely examined two-dimensional particulate flows when inertia is considered.[18,19] In FEM, the requirement of remeshing the fluid as particles move leads to increased computational costs and greater complexity of the algorithm. We choose to work with the lattice-Boltzmann method (LBM) as developed for particle-laden flows.[20–23] In the LBM, the particle and fluid motion are computed on a fixed grid, and finite inertia does not present added difficulty. The spatial locality of the lattice-Boltzmann equation and the fixed grid provide ease of parallelization. Several LB-based studies of suspensions have been reported. These include studies of two-dimensional systems (2D),[24,25] in which pair motions have been examined, as well as studies which have shown an increase in the effective

---

[a)]Electronic mail: morris@ccny.cuny.edu.

viscosity of dense suspensions with Re.[26–28] Shakib-Manesh *et al.*[26] developed a method that allows computation of the solid- and fluid-phase contributions to the total shear stress. From 2D LB simulations, they found that the shear thickening is related to the enhanced contribution from the solid phase to the total shear stress as Re increases. Following a similar approach Raiskinmäki *et al.*[27] studied the clustering of particles in a sheared suspension over the range $0 < \text{Re} \leq 10$. The authors argued that increased particle clustering with Re leads to the rise in viscosity of the suspension. Considering the detailed motions of isolated bodies, the present authors have shown that fluid inertia alters the topology of the pair trajectories in simple-shear flow.[29] The closed trajectories[30] predicted at Re=0 vanish to be replaced by spiraling and reversing trajectories.

As will be discussed in Sec. III, inertia introduces novel mechanisms for momentum transport, namely Reynolds stress due to fluctuational motion and stress due to particle acceleration. Using the LBM, we evaluate all of these to determine the total relative viscosity, normal stress differences and suspension pressure for $\phi=0.05-0.3$ and Re $=O(1)$. The results are presented in Sec. IV, preceded by the problem formulation and a description of the method for extracting the bulk stress from the simulations.

II. PROBLEM FORMULATION

A. Governing equations and computational domain

Our interest is in the motion of neutrally buoyant solid spherical particles of radius a suspended in a Newtonian fluid of density ρ and viscosity μ. The governing equations in nondimensional form for the fluid phase are

$$\nabla \cdot \boldsymbol{u} = 0, \tag{1}$$

$$\text{Re}\left(\frac{\partial \boldsymbol{u}}{\partial t} + \boldsymbol{u} \cdot \nabla \boldsymbol{u}\right) = -\nabla p + \nabla^2 \boldsymbol{u}, \tag{2}$$

where length has been made dimensionless with the radius of the sphere a, time by the inverse of the shear rate $\dot{\gamma}^{-1}$, fluid velocity by $\dot{\gamma}a$, and the pressure by $\mu\dot{\gamma}$. Particle translations ($\boldsymbol{U}_i$) and rotations ($\boldsymbol{\Omega}_i$) are governed by Newtonian dynamics,

$$m_i \frac{\partial \boldsymbol{U}_i}{\partial t} = \boldsymbol{F}_i, \tag{3}$$

$$\boldsymbol{I}_i \frac{\partial \boldsymbol{\Omega}_i}{\partial t} = \boldsymbol{T}_i, \tag{4}$$

where the net force $\boldsymbol{F}_i$ and net torque $\boldsymbol{T}_i$ act on the particle i, which has mass and moment of inertia m_i and I_i, respectively. The parameters governing the problem are the shear flow Reynolds number, defined as $\text{Re}=\rho\dot{\gamma}a^2/\mu$ and solid-volume fraction ϕ. The suspension is subjected to wall-bounded simple-shear flow. In the numerical simulations, we consider a computation box of size $L \times H \times W$ in the flow (x), gradient (y), and vorticity (z) directions, respectively, with the standard condition being $L=H=W=20a$. The x-directed shear flow is set by moving the top and bottom

walls with normal in y in opposite directions at equal speed. Periodic boundary conditions are applied in the x and z directions. We keep the domain size fixed and change the number of particles, N, to vary ϕ.

B. Lattice-Boltzmann method

The simulations utilize the lattice-Boltzmann method for particle suspensions[20,21] with later modifications.[22,23,31] We present the method briefly, and emphasize points associated with our evaluation of the bulk stress. The method combines Newtonian dynamics for the particles, as described above, with a discretized Boltzmann model for the fluid phase. The state of the system is described by the one particle velocity distribution function $n_i(\boldsymbol{r},t)$ which describes the number density of the LB particles moving with discrete velocity $\boldsymbol{c}_i$ at a lattice node $\boldsymbol{r}$ at time t. The standard lattice density used is $a=6.2$ lattice spacings. We use the D3Q19 model[23] for the set of discrete velocities. The mass density ρ and velocity $\boldsymbol{u}$ at a point in space are obtained as the moments of the velocity distribution function

$$\rho = \sum_i n_i, \quad \boldsymbol{u} = \frac{\Sigma_i n_i \boldsymbol{c}_i}{\rho}. \tag{5}$$

The time evolution of n_i consists of two steps: the collision in which the distribution relaxes toward equilibrium and the advection in which the distribution streams to neighboring nodes. This is written as

$$n_i(\boldsymbol{r}+\boldsymbol{c}_i,t+1) = n_i(\boldsymbol{r},t) + \sum_j \Omega_{ij}(n_j - n_j^{\text{eq}}), \tag{6}$$

where Ω_{ij} is the collision operator. The equilibrium distribution function n_i^{eq} is Maxwellian to recover the Navier–Stokes equations at low Mach number.[23]

We implement solid-fluid boundary conditions through the "link-bounce back" rule for the particle surfaces and the walls. In general, if a solid boundary is moving with speed $\boldsymbol{u}_b$ then the distributions at nodes adjacent to the boundary are adjusted by

$$n_{-i}(\boldsymbol{r},t+1) = n_i^*(\boldsymbol{r},t) - \frac{2a^{c_i}\rho_0\boldsymbol{u}_b \cdot \boldsymbol{c}_i}{c_s^2}, \tag{7}$$

where $-i$ denotes the velocity $\boldsymbol{c}_{-i}=-\boldsymbol{c}_i$ and c_s is the speed of sound. Note, in the above expression n_i^* is the postcollision distribution and a^{c_i} are the coefficients associated with speed c_i. In this update, momentum is exchanged between the solid and the fluid particle, and the force exerted at the boundary node ($\boldsymbol{r}_b$) is given by

$$\boldsymbol{f}_b(\boldsymbol{r}_b) = \left[2n_i^* - \frac{2a^{c_i}\rho_0\boldsymbol{u}_b \cdot \boldsymbol{c}_i}{c_s^2}\right]\boldsymbol{c}_i, \tag{8}$$

The force, torque, and the stresslet (the symmetric first moment of surface stress discussed further in Sec. III) exerted by a particle are then computed by summing over all boundary nodes as

$$F = \sum_{r_b} f_b, \quad T = \sum_{r_b} f_b \times r_b, \quad \text{and } S^0 = \sum_{r_b} \frac{1}{2}(f_b r_b + r_b f_b).$$
$$(9)$$

The LBM allows computation of these surface integrals without the need to compute the local stress.

We also incorporate lubrication forces to take into account the near-field particle-particle and particle-wall interactions. If the surface separation becomes less than a defined cutoff h_c, then the following correction force[31] is added:

$$F_{\text{lub}} = -\frac{6\pi\eta(ab)^2}{(a+b)^2}\hat{r}\hat{r} \cdot U_{21}\left(\frac{1}{h} - \frac{1}{h_c}\right),$$
$$(10)$$

where a and b are the radii of the spheres, $r = x_2 - x_1$ for particles centered at x_1 and x_2 with $\hat{r} = r/|r|$, and $U_{21} = U_2 - U_1$ is the relative velocity of the pair. The gap $h = |r| - a - b$ is between the points of closest approach of the surfaces. The stresslets due to close-pair (S^{p-p}) and particle-wall interactions (S^{p-w}) are computed similarly by making use of the asymptotic forms of hydrodynamic interaction functions as tabulated by Kim and Karrila,[32] with greater details available from Nguyen and Ladd.[31] The total particle stresslet is then given by

$$S_i = S_i^0 + S^{p-p} + S^{p-w}.$$
$$(11)$$

It is relevant to note that the LBM, as employed here, allows slight fluid compressibility. The Mach number is thus nonzero, and is defined $\text{Ma} = \dot{\gamma}H/(2c_s)$, where $\dot{\gamma}H/2$ is the wall velocity. We maintain $\text{Ma} < 0.1$ in all calculations presented here in order to minimize compressibility effects. The influence of varying Ma on pair trajectories at finite Re is addressed in other work.[29]

III. AVERAGE SUSPENSION PROPERTIES

To determine the full set of viscometric functions associated with the simulated shear flow, we apply the procedure developed by Batchelor[1] to compute the bulk stress generated by a flowing suspension in terms of volume averages. In this formulation, the suspension is considered as statistically homogeneous, implying the average properties of a suspension in volume V, containing many particles, do not vary appreciably. The presence of boundaries in the system studied implies some spatial variation and we address the limitations associated with this below.

The volume and surface of a typical particle are denoted by V_p and A_p, respectively. At a material point x, we denote by u and σ the velocity and stress fields, respectively. Without any restriction on solid-volume fraction and Reynolds number of the motion, the bulk stress (nondimensionalized by $\mu\dot{\gamma}$) can be written as

$$\Sigma = \frac{1}{V}\int_{V_f} -pI dV + (\nabla U + \nabla U^T) + \Sigma^p,$$
$$(12)$$

where V_f is the volume occupied by the fluid, and ∇U is the volume average of the local velocity gradient. Σ^p denotes the particle contribution to the bulk stress and is given by

$$\Sigma^p = \frac{1}{V}\sum_i S_i - \frac{\text{Re}}{V}\sum_i \int_{V_p} \frac{1}{2}(ax + xa)dV_i - \frac{\text{Re}}{V}\int_V u'u' dV,$$
$$(13)$$

where summations are over all the particles in volume V. The first term represents the stresslet, or symmetric first moment of surface stress, exerted by a particle i, given for a rigid particle by

$$S_i = \int_{A_p} \frac{1}{2}(x\sigma \cdot n + \sigma \cdot nx)dA_i,$$
$$(14)$$

where n is the normal directed outward from the particle surface into the fluid phase. The second and third terms in the expression of particle stress denote the stress due to acceleration of the particles and the Reynolds stress, respectively. The acceleration stress originates from the nonlinear convective terms $u \cdot \nabla u$ in the Navier–Stokes equations. Note that the acceleration of the material point x residing in particle i is $a = a_i + \alpha_i \times x + \Omega_i \times (\Omega_i \times x)$, where a_i and α_i are linear and angular accelerations of the particle. The presence of particles disturbs the mean bulk motion of the fluid ($\bar{u}$) and the resulting velocity fluctuations ($u' = u - \bar{u}$) at the microscale cause momentum transfer across a surface element. These velocity fluctuations are concealed by the averaging process, but are taken into account through the Reynolds stress.[1] The expression (13) directly shows that the contributions to the bulk stress from the acceleration and Reynolds stress are dependent on Re; the stresslet is dependent on Re through the flow solution. For a dilute suspension, the interactions between the particles can be neglected and the solution for a single particle can be used to calculate the particle stress. Using matched asymptotic expansions, Lin et $al.$[17] obtained the flow field around a single particle at small but finite Re and deduced that inertia gives rise to normal stresses with a negative first normal stress difference and positive second normal stress difference. Finite element calculations[33] confirm the validity of the theory at $O(\text{Re})$.

It is an objective of this study to calculate the particle stress (Σ^p) for a suspension in simple-shear flow over a range of ϕ and Re. At each time step, the acceleration and Reynolds stresses are computed from the knowledge of particle velocities and the velocity field. The stresslets are computed from Eq. (11). The time-averaged quantities of interest are relative viscosity μ_r, the normal stress differences N_1 and N_2, and the particle pressure Π, defined as

$$\mu_r = 1 + \frac{\langle\Sigma_{xy}^p\rangle}{\mu\dot{\gamma}},$$
$$(15)$$

$$N_1 = \langle\Sigma_{xx}^p\rangle - \langle\Sigma_{yy}^p\rangle,$$
$$(16)$$

$$N_2 = \langle\Sigma_{yy}^p\rangle - \langle\Sigma_{zz}^p\rangle,$$
$$(17)$$

and

$$\Pi = -\frac{1}{3}(\langle\Sigma_{xx}^p\rangle + \langle\Sigma_{yy}^p\rangle + \langle\Sigma_{zz}^p\rangle),$$
$$(18)$$

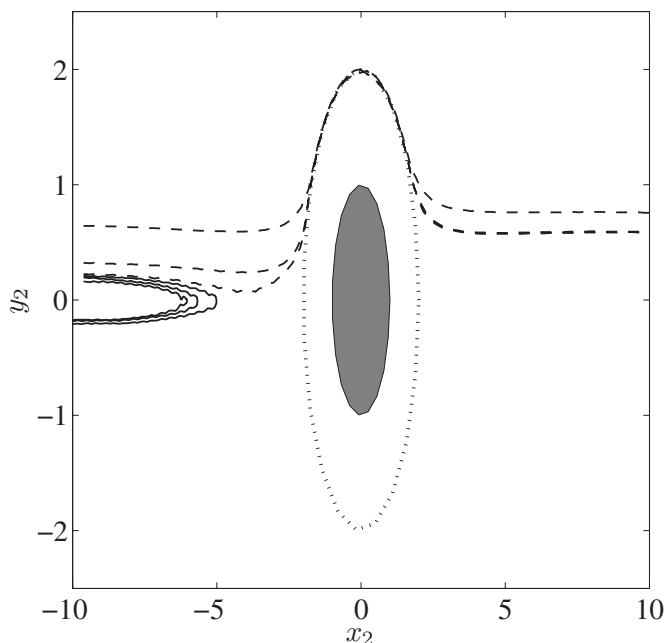where $\langle\ \rangle$ denotes the time-averaged quantity.

FIG. 1. In-plane trajectories of a pair of equal-sized spheres of radius 1 in simple-shear flow at Re=0.1 starting at the same streamwise but different gradient separations. Open trajectories are denoted by dashed lines and reversing by solid lines. The dotted and shaded ellipses denote the excluded volume and the particle at the origin, respectively; these are elliptical because of the stretched y coordinate.

IV. SIMULATIONAL RESULTS

A. Pair trajectories at finite Re

We begin by briefly reporting the nature of pair trajectories of two equal radii spheres at finite fluid inertia, with greater detail and unequal pair trajectories available elsewhere.[29] The trajectory space is sampled by varying the initial positions of the spheres, with the pair symmetrically placed about the central point in the computational domain. For any initial separation, the initial condition on the trajectory is set by allowing the spheres to rotate until they are torque-free and the flow field is steady, at which time the particles are released. We describe the pair trajectories in terms of the time variation of the separation of the centers of the pair of spheres, $r(t) = x_2(t) - x_1(t)$, with initial separation denoted by $r_0 = (r_{0x}, r_{0y}, r_{0z})$.

Fluid inertia alters the topology of the trajectories of neutrally buoyant particles relative to the Stokes flow results: the trajectory space transitions from having two regions (open and closed) at Re=0 to three types at any finite Re. These three trajectory types mirror the form of the streamlines[33–35] of the steady finite-Re flow around a sphere and are termed open, reversing and spiraling.

The *open trajectories* at finite Re are similar to those predicted for the Stokes flow, starting from upstream infinity and progressing in the x (streamwise) direction in the same sense at every point, with inertia inducing some deflection of the pair toward the same y when the pair is close. In the *reversing trajectories*,[33,34] a pair starting with an initial offset of $r_x < 0$ and $r_y > 0$ approaches, reverses relative positions in y, and recedes toward $r_x < 0$ and $r_y < 0$. Figure 1 illustrates open and reversing trajectories in the plane of shear at

Re=0.1, beginning with a small r_{0y} and $r_{0x} = -9.7$. The open trajectory shows evidence of fluid inertia, as there is a deflection toward the zero-velocity ($y = 0$) plane upon close approach, and a net positive displacement in the gradient direction ($\Delta y > 0$) through the complete interaction. With increasing Re, there is a larger region in y of initial conditions which undergo the reversal, while the pair also approach more closely before reversal.

On *spiraling trajectories*, out-of-plane pairs at finite r_{0z} lying near the vorticity axis (z) approach one another along a path which spirals outward when projected onto the x-y plane, eventually moving away in x. If the two particles lie in the shear plane, for Re ≥ 0.1, a very small separation is necessary to see the spiral. At lower Re, the reversing trajectories do not approach the contact surface so closely and hence spiraling trajectories become readily visible. Figure 2 illustrates in-plane and out-of-plane spiraling trajectories for equal radius spheres in simple-shear flow.

B. Bulk stress

Here, we provide the numerically determined bulk rheological properties of suspensions at varying ϕ and Re. Simulations start with the particles placed randomly in the simulation domain. The walls are set in motion with the mixture in a resting state. We simulate flows which generate total strains of $\dot{\gamma}t = 100-300$ depending on Reynolds number. Data from the first 20–30 strain are discarded so that the initial condition and bulk acceleration do not affect the reported properties. We present the time-averaged properties for $0.01 \leq \text{Re} \leq 2$ and for $0.05 \leq \phi \leq 0.3$, with these solid fractions corresponding to $N = 77-516$ particles in the unit cell. Rheological quantities are calculated using Eqs. (13) and (15)–(18). Before addressing the bulk rheology, we present the solid-volume fraction (ϕ_y) and the axial velocity (u_x), averaged over time and planes parallel to the walls as a function of y, the cross-stream coordinate. The results are shown in Fig. 3 for a suspension at Re=0.1, with the plots arranged with y running vertically to suggest a horizontal channel. Note that the volume fraction is based on the center positions of the particles, resulting in zero ϕ near the walls. At lower ϕ, a weak migration toward the center is seen, but the velocity profile is little changed from that of a linear shear flow. At $\phi = 0.3$, strong layering of particles near the walls is observed. The shear rate is no longer homogeneous near the walls and a relatively lower shear rate exists in the middle of the channel. There is, thus, a slip velocity on a macroscopic scale. This profile is found to develop at $\dot{\gamma}t \approx 20$ and is used for $\bar{\mathbf{u}}$ in the calculation of Reynolds stress (13).

In Fig. 4(a), we plot the relative viscosity of the suspension as a function of ϕ for various Re. Also shown in the figure are the Eiler fit[3,36]

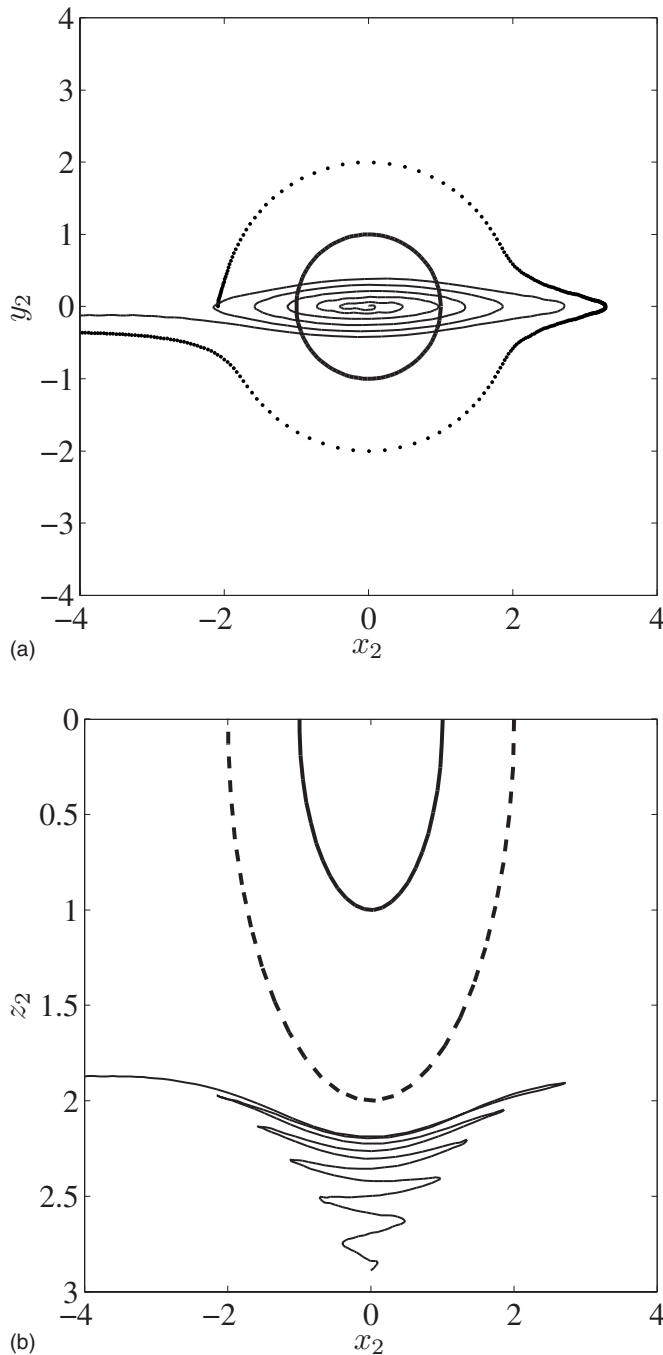$$\mu_r(\phi) = \left[1 + \frac{1.5\phi}{(1 - \phi/\phi_m)} \right]^2, \tag{19}$$

FIG. 2. Out-of-plane spiraling trajectory (solid line) starting from r_0 $=(-0.0032, 0.016, 2.9)$ for Re=0.1 and in-plane spiraling trajectory (dotted line) originating from $r_0=(-2.16, 0, 0)$ for Re=0.01 in simple-shear flow, (a) xy projection (b) xz projection of the out-of-plane trajectory. The thick solid line in both panels represents the particle, while the dashed line in (b) denotes the excluded volume to indicate closeness of surfaces.

FIG. 3. The time-averaged (a) axial velocity and (b) local solid-volume fraction ϕ_y along the height in a sheared suspension at Re=0.1 and for ϕ =0.05 and 0.3. Note that ϕ_y is based on the center positions of the particles, and u^∞ is the undisturbed shear flow.

with $\phi_m=0.58$ and the dilute-limit analytical result of Batchelor and Green[37] $(\mu_r=1+2.5\phi+7.6\phi^2)$, both of which are applicable at low Reynolds number. The viscosities compare well with these curves for $\phi \lesssim 0.2$. However μ_r departs from these predictions at higher ϕ. We have computed the viscosity directly from the shear force on the walls, as μ_r $=F_{x,\text{wall}}/(2\mu u_w/H)$, where u_w is the wall speed and H is the wall separation, in addition to the method outlined in Sec. III. Viscosities at Re=0.1, obtained from the two approaches
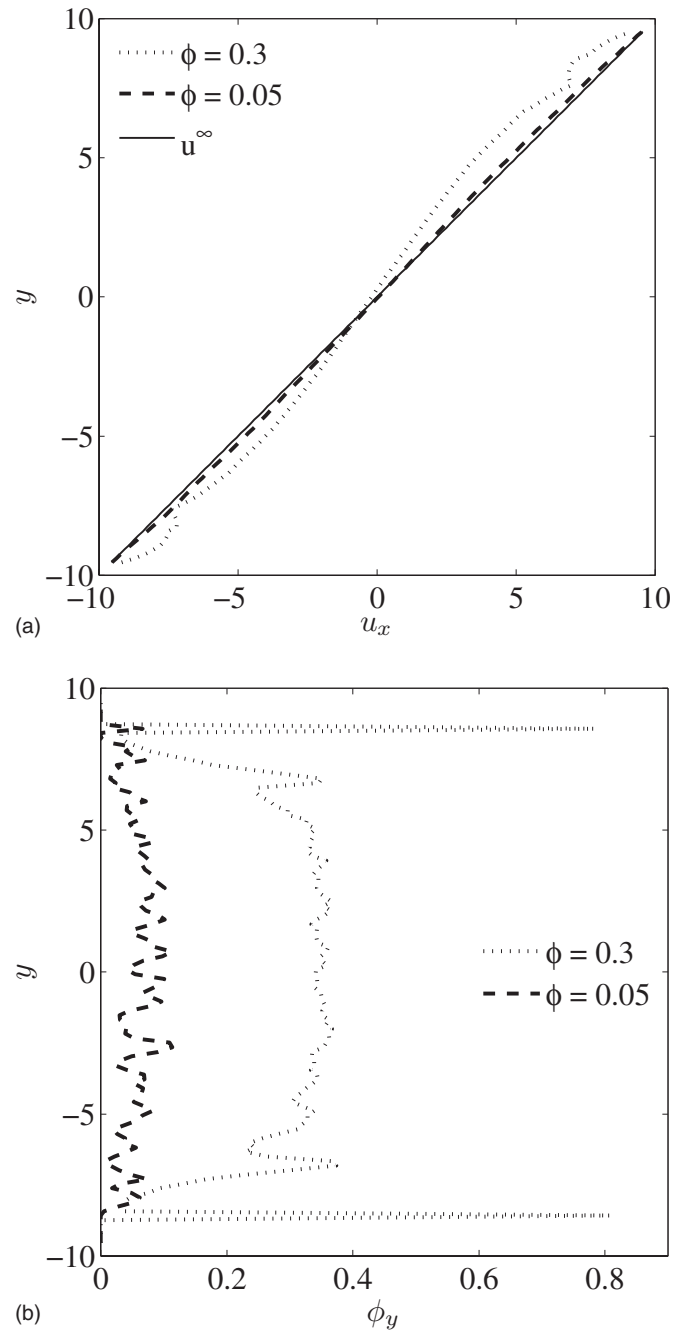
for ϕ=0.05 and 0.3 are shown in Fig. 5 for an extended period of dimensionless time. For ϕ=0.05, we obtain a good agreement between the two results whereas for ϕ=0.3 deviations as large as 10% are observed, with the result based on the wall shear stress larger owing to the reduced shear rate acting on the interior particles. The equivalent boundary calculation for normal stress differences is less direct and is not performed here. The effect of Re on the relative viscosity is shown in Fig. 4(b), where we present μ_r as a function of Re for different ϕ. The general trend observed is that the viscosity of the suspension increases, *i.e.*, it shear thickens with Re,
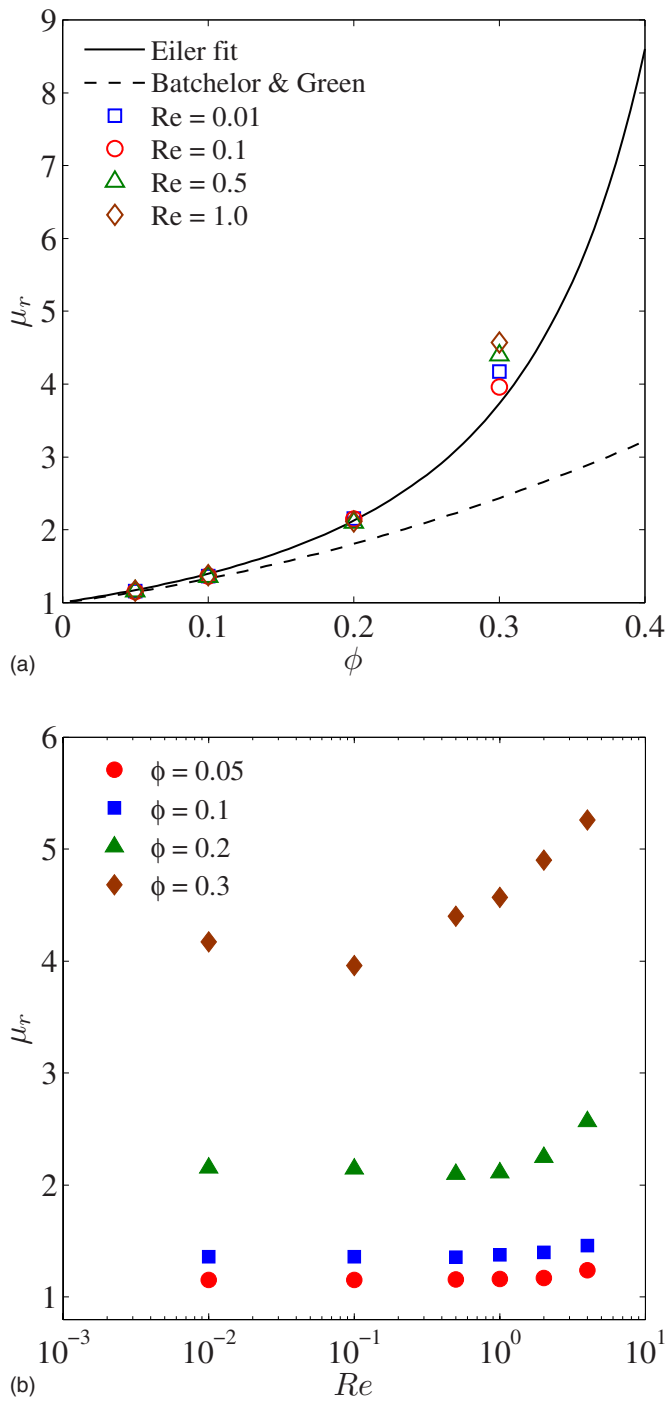
FIG. 4. (Color online) (a) The relative viscosity of a monodisperse suspension as a function of solid-volume fraction. The Re=0 empirical model of Eiler (Ref. 3) and analytical result of Batchelor and Green (Ref. 37) are also shown. (b) The dependence of relative viscosity on Re for $0.05 \leq \phi \leq 0.3$.

FIG. 5. (Color online) (a) The instantaneous relative viscosity of a sheared suspension at Re=0.1 obtained from the bulk stress calculation and from the shear stress on the walls for (a) $\phi=0.05$ and (b) $\phi=0.3$, the legend applies to both plots.

for Re > 0.1. The thickening for the range of Re considered here is not prominent at lower volume fractions, in agreement with results of 2D LB simulations of Kromkamp *et al.*[24] and Shakib-Manesh *et al.*[26] It is also of interest to note that for $\phi=0.3$, there is a small drop in the viscosity for low Re. The contributions from the acceleration and Reynolds stresses to the viscosity are found negligible compared to the stresslets, although both of them rise linearly with Re. We suggest that it is the combined effect of some ordering of
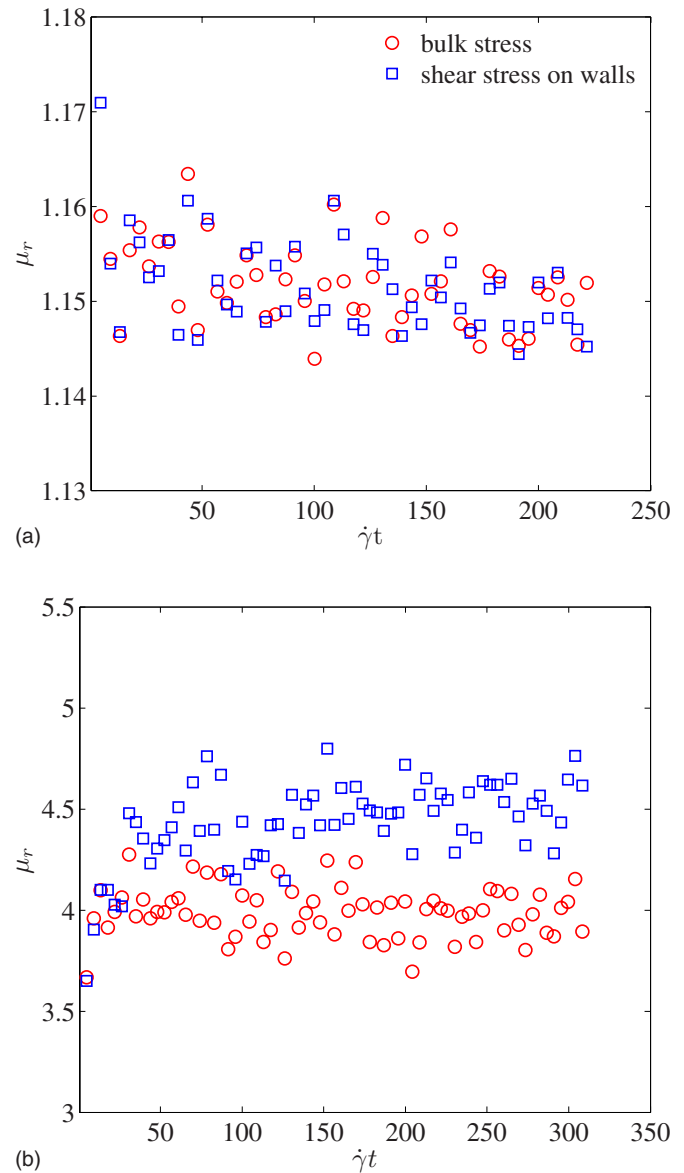
the microstructure along the flow direction (as will be seen in Sec. IV C) and increased single particle stresslet[33] at higher Reynolds numbers which leads to the drop and rise of the viscosity.

The first and second normal stress differences scaled by $\mu\dot{\gamma}$ are presented in Fig. 6 along with Re=0 values predicted by accelerated Stokesian Dynamics (ASD) simulation.[13] In the ASD simulations, a short range interparticle force was used to prevent overlaps of particles and it was found that both N_1 and N_2 are negative for all ϕ and $N_1 \approx N_2$. To our knowledge, no experimental data on normal stresses are available for $\phi < 0.3$, but it is worth noting that the experimental results for viscous conditions of Zarraga *et al.*[3] agree with the simulations in finding both N_1 and N_2 negative, but $|N_2|/|N_1| \approx 3.6$ from the correlation of experimental data at large ϕ. For finite Re, theoretical predictions[17] are available
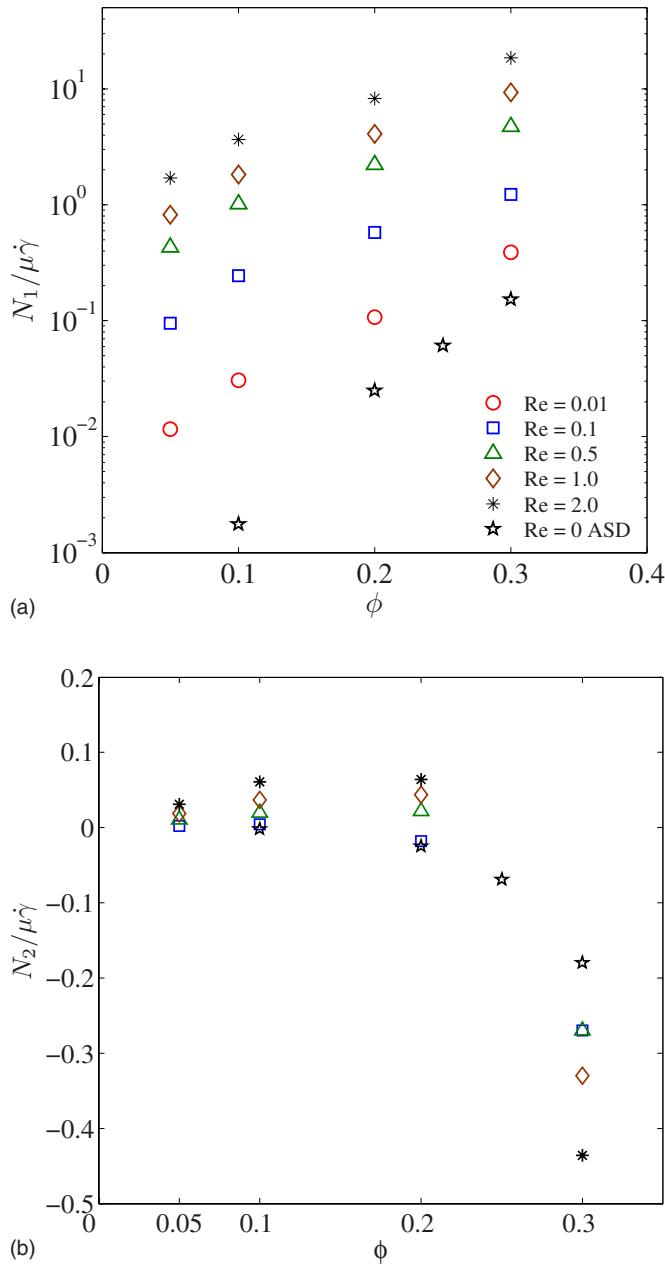
FIG. 6. (Color online) The dependence of normal stress differences on solid-volume fraction: (a) N_1 and (b) N_2. Also shown are ASD simulation results for Re=0. The legend applies to both plots.

FIG. 7. (Color online) The dependence of normal stress differences on Re for $0.05 \leqslant \phi \leqslant 0.3$: (a) N_1 and (b) N_2. The legend applies to both plots.

only in the limit of $\phi \rightarrow 0$, with $N_1 < 0$ and $N_2 > 0$, and both of $O(\text{Re})$. For the range of ϕ considered in this study, N_1 is negative and $|N_1|$ increases with ϕ. At Re=0.01, N_1 compares well with ASD simulation results for $\phi \geqslant 0.2$. At smaller ϕ, however, N_1 is relatively greater than the ASD values, possibly because, at finite Re, the single particle contributes a finite normal stress difference. In the case of N_2, we observe a change in the sign. For $\phi \leqslant 0.1$, N_2 is positive for the entire range of Re, consistent with the theoretical predictions of Lin *et al.*[17] However, for a suspension with $\phi=0.2$, N_2 is negative for Re$\leqslant 0.1$ and positive for Re $\geqslant 0.5$. For $\phi=0.3$, N_2 is negative for all Re.

The Re dependence of N_1 and N_2 is shown in Fig. 7; the inset shows N_2 for $\phi=0.05$ and 0.1. At low ϕ, both normal
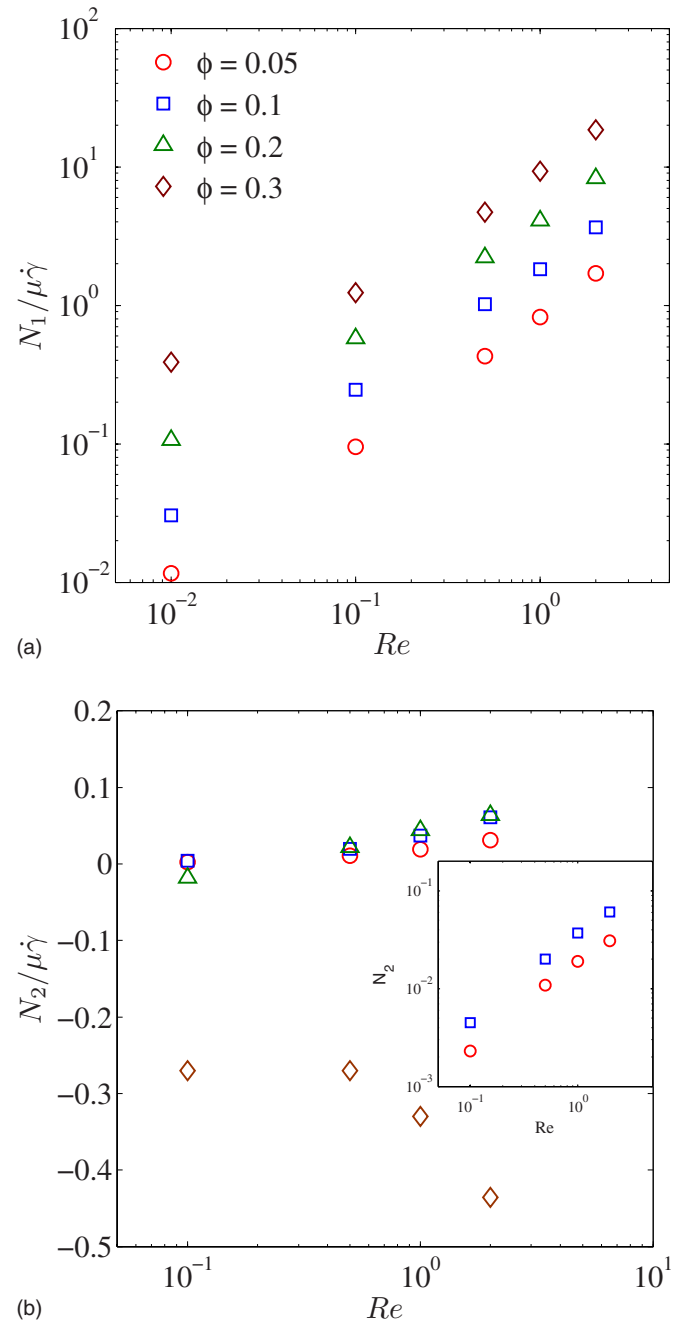
stress differences scale linearly with Re, in agreement with theoretical predictions[17] and numerical evaluation for a single sphere.[33]

The particle pressure (Π), presented in Fig. 8, rapidly increases with ϕ. The agreement between LB simulations for Re=0.01 and ASD results at Re=0 is good at higher volume fractions. Similar to N_1 and N_2, the particle pressure is also found to be roughly $O(\text{Re})$ for small ϕ for the range of Re studied [see Fig. 8(b)].

Before closing this section, we note that the numerical simulations suffer from certain limitations. First, in the LB method, the particle surface is represented by lattice nodes, and hence one needs to choose a sufficiently large lattice
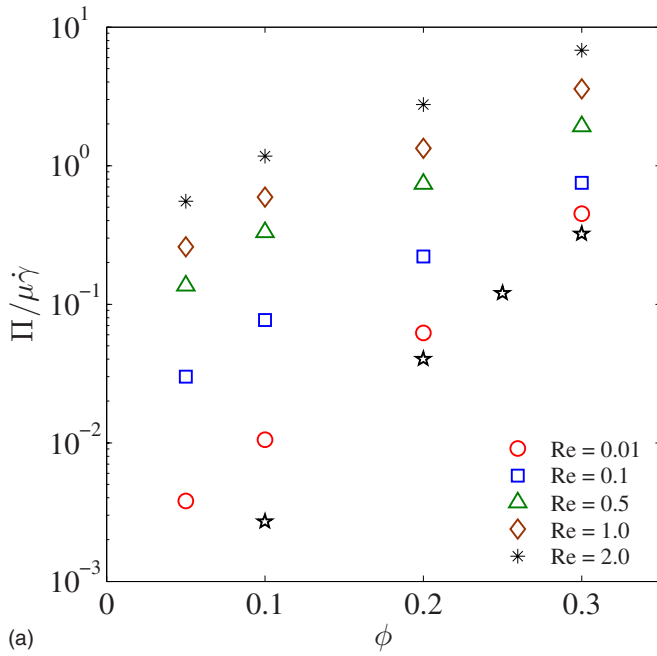
(a)
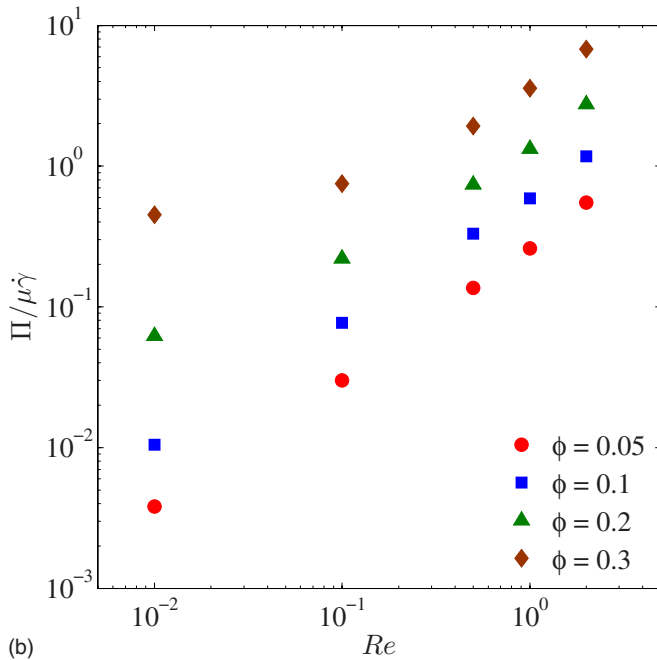
(b)

FIG. 8. (Color online) The particle pressure as a function of (a) solid-volume fraction and (b) Re. Also shown in (a) are ASD simulation results for Re=0.

FIG. 9. Definitions of the polar angle θ and the azimuthal angle ψ in simple-shear flow $\boldsymbol{u}=(\dot{\gamma}y,0,0)$.

C. Microstructure

We consider the pair microstructure at finite Re in the simulated shear flows from which the foregoing stress results are obtained. The microstructure is described by the pair distribution function, defined as

$$g(\boldsymbol{r}) = \frac{P_{1|1}(\boldsymbol{r}|\boldsymbol{0})}{n}, \tag{20}$$

where n is the average particle number density and $P_{1|1}(\boldsymbol{r}|\boldsymbol{0})$ is the conditional probability of finding a particle at $\boldsymbol{r}$, given one at the origin $\boldsymbol{0}$. From the simulations, $g(\boldsymbol{r})$ is calculated as follows.[12] The pair space is discretized in (r,θ,ψ) with these coordinates sketched about a reference particle in Fig. 9, where θ is the polar angle, measured from the positive x axis and ψ is the azimuthal angle, measured from the positive z axis. At each sampling time, from the simulated particle configurations, we obtain $N(N-1)/2$ pair separation vectors $\boldsymbol{r}$, where N is the number of particles. Each vector $\boldsymbol{r}$ is put into respective bin of volume $\Delta V = r^2 \Delta r \sin \psi \Delta \psi \Delta \theta$ and a running histogram $H(r,\theta,\phi)$ is built. The pair distribution function g is then calculated as

$$g(r,\theta,\psi) = \frac{H(r,\theta,\psi)}{n t_s \Delta V}, \tag{21}$$

where t_s is the total number of sampling points.

The particular goal here is to identify effects of fluid inertia on the microstructure in the shear. We first consider the radial distribution function $g(r)$, which is $g(r,\theta,\psi)$ averaged over all possible orientations. Results are presented for $0.01 \leqslant \mathrm{Re} \leqslant 2$ and $0.05 \leqslant \phi \leqslant 0.3$. At higher ϕ, particles build up near contact because of volume exclusion and, hence, it is difficult to see the signature of inertia in $g(r)$. The inertial effects are expected to become more readily visible at smaller ϕ. In Fig. 10, we plot $g(r)$ for $\phi=0.05$ at different Re along with the theoretical prediction for dilute ϕ and Stokes

density. Second, the motion is simulated in a periodic and wall-bounded domain; the bulk properties depend to some degree on L, W, and H for a chosen mesh density of the sphere. The dependence on the number of particles N is equivalent to the dependence on the domain size. Effects of periodicity and domain size are not negligible at smaller volume fractions and that may explain discrepancy between LB results at Re=0.01 and ASD results. Finally, finite compressibility is inherent in the LB method, but as long as Ma <0.1, it does not generate qualitative differences and the quantitative effects are believed to be small.
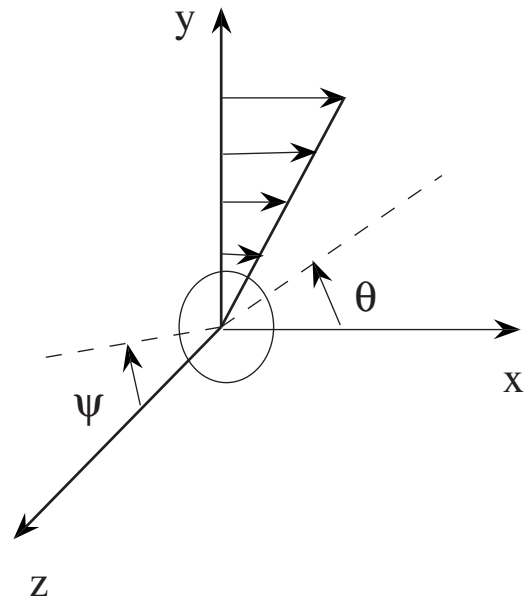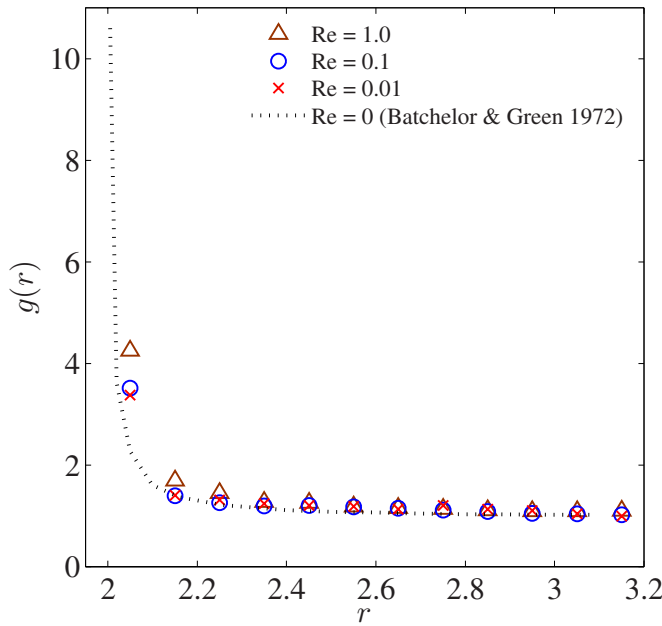
FIG. 10. (Color online) The pair distribution function $g(r)$ determined from LB simulations for a sheared suspension of $\phi=0.05$ for Re=0.01,0.1, and 1.0.

FIG. 11. (Color online) The angular dependence of pair distribution function at contact in the plane of shear for a suspension at Re=0.1 for $0.05\leqslant\phi\leqslant0.3$ determined from LB simulations.

flow of Batchelor and Green,[37] which predicts that $g(r)$ is divergent at contact. The figure shows that, except near contact, the theoretical $g(r)$ remains smaller than the simulated values at finite Re, and $g(r)$ near contact increases with Re.

Next, we consider the angular variation of $g(\mathbf{r})$ adjacent to contact in the plane of shear ($\psi=\pi/2$). We recall that, at Re=0, $g(\mathbf{r})$ is fore-aft symmetric in the dilute pure hydrodynamic limit owing to the reversibility of Stokes equations. The symmetry can be broken by the Brownian motion, interparticle forces, or finite Re. In this study, we are not considering the effect of the former two. The size of bin for r used here is relatively large at $\Delta r=0.1$ to rapidly populate all bins at smaller volume fractions. Figure 11 shows angular variation of $g(2\leqslant r\leqslant2.1,\theta)$, termed $g(2)$, at Re=0.1 for $0.05\leqslant\phi\leqslant0.3$. Note that $\theta>90°$ and $\theta<90°$ correspond to the compressional and extensional quadrants, respectively. The anisotropy in the pair microstructure is visible at all ϕ with elevated pair density in the compressional quadrant. However, $g(2)$ is almost constant in the range $\theta=50°-130°$, or 40° to each side of the natural point of symmetry, 90°. As ϕ increases, pair probability accumulates along the flow axis, i.e., near $\theta=0°$ and $\theta=180°$. At $\phi=0.3$, the primary peak is observed along the flow axis.

The Re dependence of $g(\mathbf{r})$ near contact is shown in Fig. 12, where we plot $g(2)$ in the plane of shear at $\phi=0.1$ for $0.05\leqslant\text{Re}\leqslant2$. Also shown in the figure are the Re=0 result obtained using Stokesian Dynamics simulations by Drazer et al.[38] for which the values are averaged over all ψ and, for comparison, the LB result at Re=0.05 likewise averaged over ψ; the data for the two cases are generally similar, and, in fact, differs very little over the angular range $50°<\theta<150°$, with the finite-Re results somewhat elevated relative to the Stokes-flow results at the angles closer to the flow axis. Near symmetry of pair microstructure is seen at Re=0
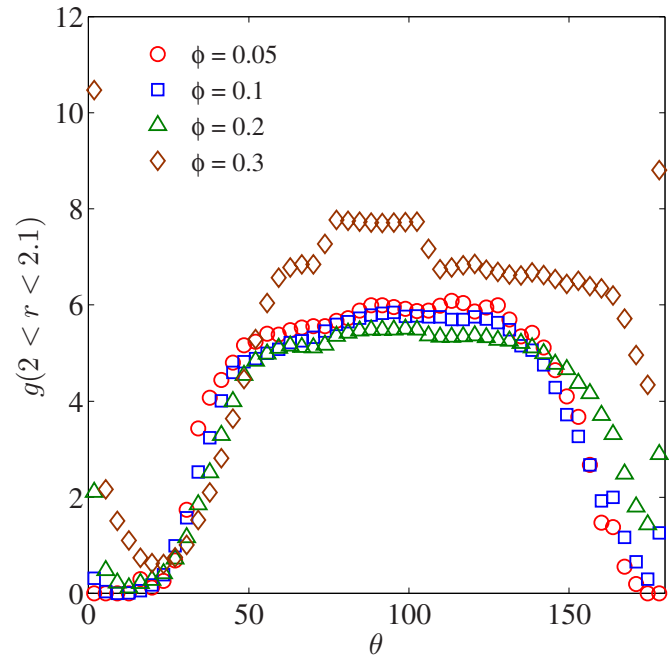
and as Re increases, the asymmetry in $g(2)$ substantially increases. In fact, for Re=2, the sampled pair probability at contact is zero for $5°\leqslant\theta\leqslant40°$: no pairs were found in the near-contact region ($2\leqslant r\leqslant2.1$) for this range of angles. The maximum value of $g(2)$ observed over the contact surface also rises with Re.

The case of a suspension at $\phi=0.3$ is considered in Fig. 13. Again, asymmetry in $g(2)$ is observed to increase with
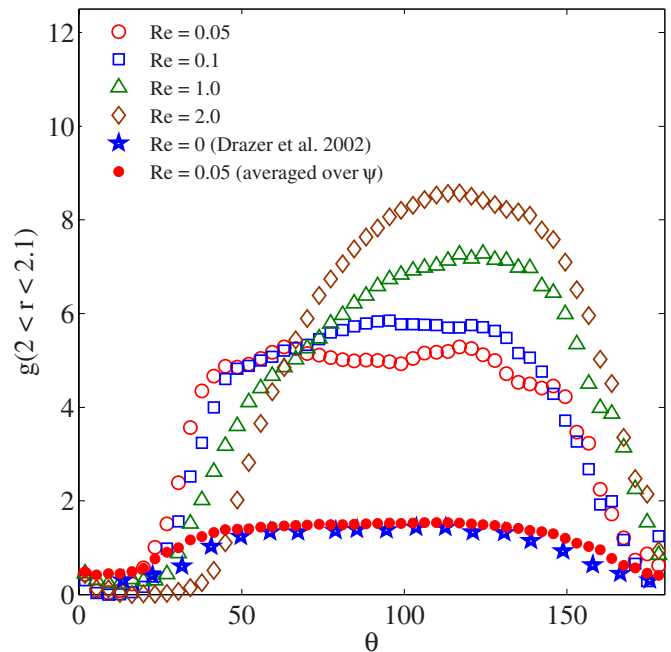

FIG. 12. (Color online) The angular dependence of pair distribution function at contact in the plane of shear for a suspension of $\phi=0.1$ for $0.1\leqslant\text{Re}\leqslant2.0$.
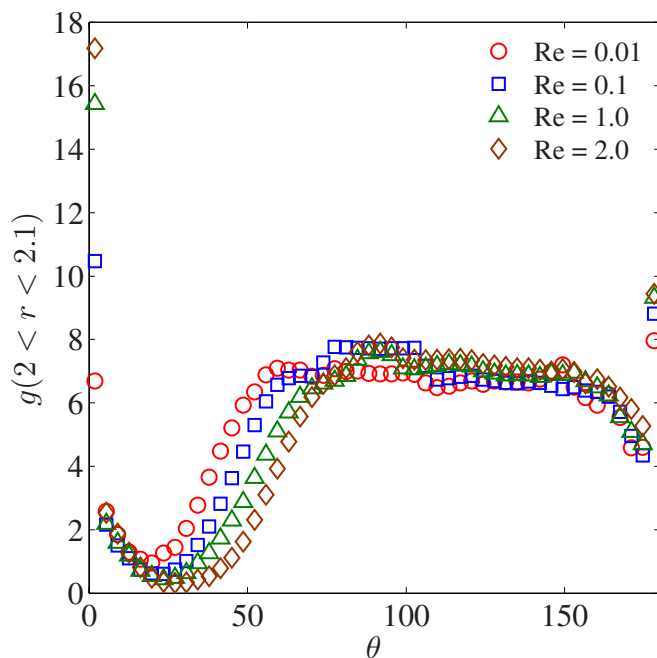
FIG. 13. (Color online) The angular dependence of pair distribution function at contact in the plane of shear for a suspension of $\phi=0.3$ for $0.1 \leqslant \text{Re} \leqslant 2.0$.

Re, but the maximum value in the broad high-correlation region of the compressional quadrant does not vary in magnitude with Re. The notable variation in magnitude is that $g(2)$ along the flow axis increases quite rapidly with Re. This is not due to layering of particles near the wall, as layering is observed for all Re. Based on finite Re pair motion as mentioned in the Sec. IV A, reversing trajectories may play a role in this structure, but we recall that, at $\phi=0.3$, the average surface separation between particles is well below a particle radius.

Finally, we note points where the pair microstructure may provide insight to the bulk rheology. The relationship is not so readily determined in a finite-Re suspension as in the case of Re=0, as the stress associated with even an isolated pair interaction requires a time-consuming sampling of the pair space at the Re of interest, and this information is not yet available. However, certain known features of the single particle and interacting pair at finite Re may guide understanding. At low volume fractions ($\phi=0.05$ and 0.1), a particle spends a significant fraction of the time well separated from others and the theoretical predictions[17] for an isolated particle at finite Re appear to hold, namely, we obtain negative N_1 and positive N_2 with both quantities scaling linearly with Re. At $\phi=0.3$, however, the dominant contribution to the bulk stress comes from the particles near contact. Even at low Re, there is a depletion of the pair probability on the downstream side of the pair interaction. If we now recall N_1 and N_2 as a function of pair orientation[3] within the plane of shear, described by θ, it appears that the structural asymmetry leads to negative N_1 and N_2.

D. Velocity fluctuations

In this section, we present probability density functions (PDFs) of particle velocities in the gradient (U_y) and vorticity (U_z) directions. A single particle freely suspended in a simple-shear flow will move with the streamline at its center. The presence of a second particle forces a departure from the streamline, and U_y and U_z become nonzero. The statistics of these velocity fluctuations are probed here. The velocity PDFs fit a general form

$$P(U_i) \propto \exp[-\beta|U_i|^\alpha], \tag{22}$$

where $i=y$ or z, and β is a fitting parameter. The value of $\alpha=1$ corresponding to an exponential distribution is found to describe low-ϕ data reasonably well, while $\alpha=2$ corresponding to a Gaussian distribution is found at our largest ϕ. We do not attempt a complete fitting of the data at all conditions, as values of α intermediate between 1 and 2, as well as a mixture of the two distributions may be seen in different cases. Instead, we present the data from a number of conditions and note the fitting to selected limiting cases. Figure 14 shows the measured PDF for U_y and U_z for $\phi=0.05$, 0.1, 0.2, and 0.3 at Re=0.1. Note that particles near the walls (surface separation from the wall less than a particle diameter) are not taken into account, and the velocities are scaled as $\dot{\gamma}a$ using the bulk average shear rate. The width of $P(U_y)$ increases with ϕ and we see a gradual transition from an exponential to a Gaussian distribution as ϕ increases. The PDFs at Re =0 obtained using Stokesian Dynamics simulations[38] exhibit a similar transition with ϕ: Drazer et al. argued that the addition of essentially random lubrication interactions at higher volume fraction is dominant in determining the dynamics of suspended particles at high ϕ and leads to a Gaussian PDF. At low ϕ, the particles may interact in a correlated fashion over extended periods with neighboring particles through long-range hydrodynamic fields and this results in a quite different exponential distribution.

We plot in Fig. 15 the PDFs for $\phi=0.05$ at Re=0.01 and 1. The data at Re=0.01 fit expression (20) with $\alpha=1$ and $\beta=11$. It also shows a good agreement with Drazer et al.[38] who obtained $\alpha=1$ and $\beta=11.4$ at Re=0 and $\phi=0.05$. We limit presentation of data to Re=0.01 and 1.0 for clarity. At the higher Re, the distribution becomes narrower. Of added interest is the bell-shaped distribution at Re=1.0 which has a sharp peak near $U_y=0$. In the case of U_z, the PDF also becomes narrower with Re but no sharp peak is found at Re=1.0. We consider the distributions at $\phi=0.3$ in Fig. 16. The distribution is of Gaussian nature for U_y and decreases in width at higher Re. For U_z, however, a Gaussian distribution fits the data for small velocity fluctuations, and an exponential distribution describes the data well for large fluctuations.

V. CONCLUSIONS

In this work, we have studied the behavior of a sheared neutrally buoyant suspension at conditions yielding finite inertia at the particle scale. The numerical simulations were performed using the lattice-Boltzmann method in a wall-bounded geometry with periodicity in the flow and vorticity
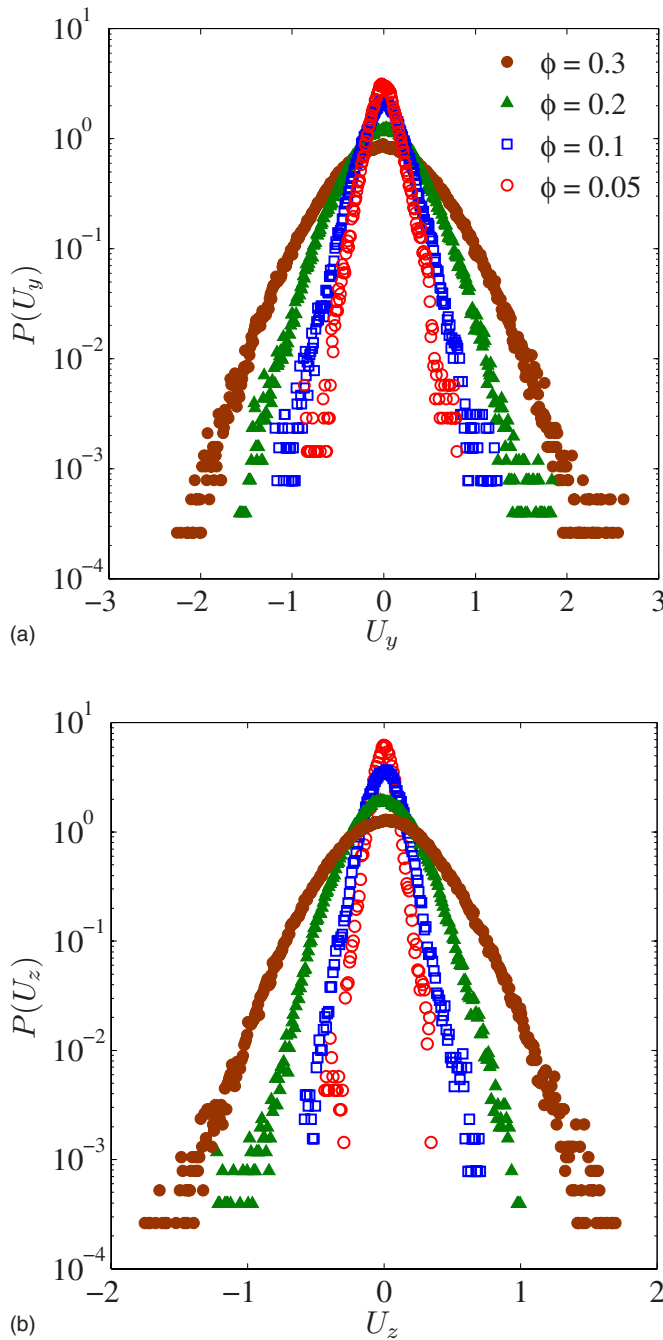
FIG. 14. (Color online) The probability density function of velocity fluctuations in the (a) gradient (y) and (b) vorticity (z) directions obtained by the LB simulations for a sheared suspension at Re=0.1 for various volume fractions.

FIG. 15. (Color online) The probability density function of velocity fluctuations in the (a) gradient and (b) vorticity directions obtained by the LB simulations for a sheared suspension at Re=0.01 and 1.0 and ϕ=0.05.

directions. The study was restricted to dilute to moderately concentrated suspensions with $0.05 \leqslant \phi \leqslant 0.3$ and inertia at a particle-scale Reynolds number of Re=$\rho\dot{\gamma}a^2/\mu$ varying in the range of $0.01 \leqslant$ Re $\leqslant 5$. We have extracted from the simulations a number of quantities of interest from a suspension mechanical perspective, including bulk rheology, pair microstructure, and velocity fluctuations.

Using Batchelor's formulation of the bulk stress, the results in this study show that inertia increases the particle contribution to the effective viscosity of the suspension and gives rise to a particle-phase normal stress. The signs of first
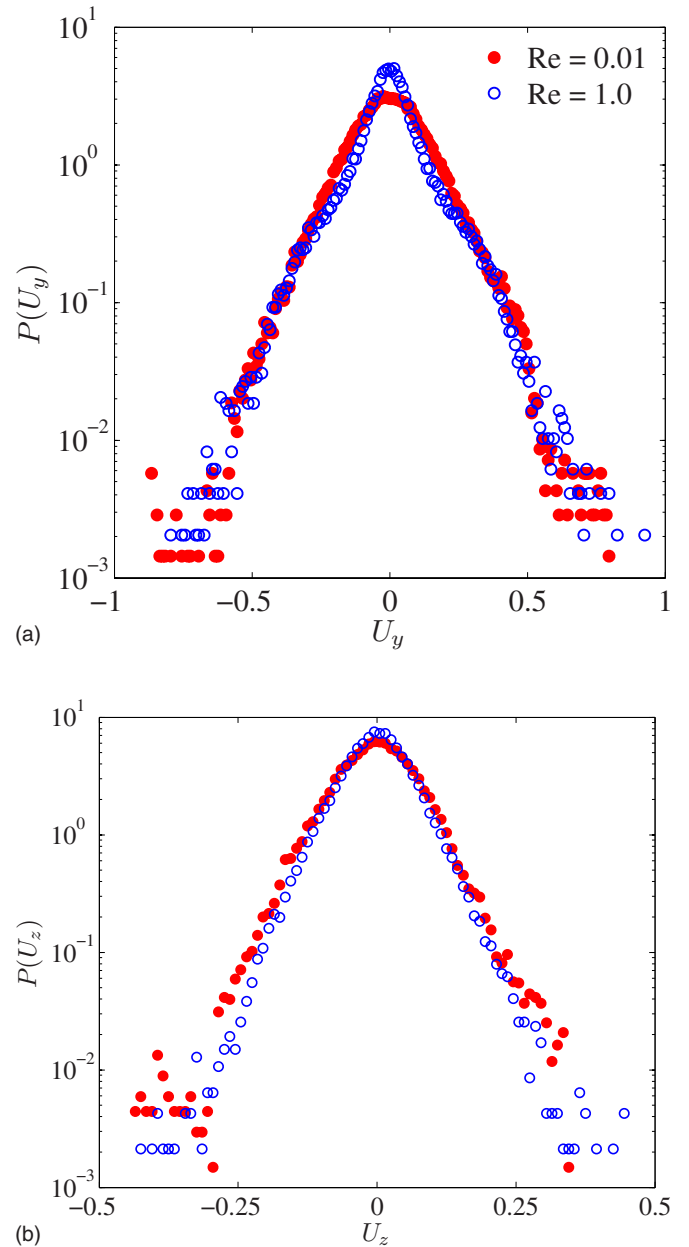
(negative) and second (positive) normal stress difference for $\phi \leqslant 0.1$ are consistent with the dilute-limit low Reynolds number theory[17] and numerics,[33] and both increase in magnitude linearly with Re. A change in sign of N_2 is observed, as it becomes negative for ϕ=0.3. The particle pressure is positive for all ϕ and also scales linearly with Re.

Inertia breaks the fore-aft symmetry of the pair distribution function seen at dilute ϕ and Re=0. The result is an anisotropic pair microstructure with elevated near-contact pair correlation in the compressional quadrant of the shear flow; the degree of asymmetry grows with Re. The microstructure found from the simulation undergoes a change at ϕ=0.3, as the primary peak is observed along the flow axis rather than in the compressional quadrant as seen at dilute ϕ. Such changes appear to qualitatively affect the non-
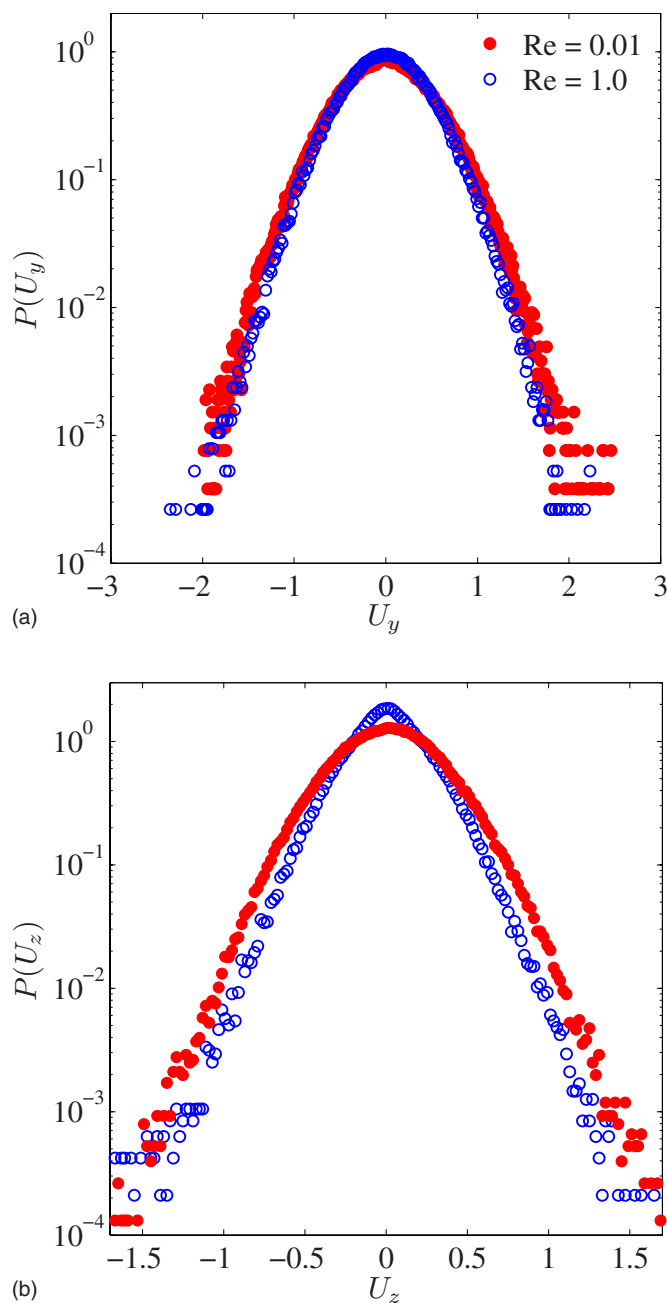
FIG. 16. (Color online) The probability density function of velocity fluctuations in the (a) gradient and (b) vorticity directions obtained by the LB simulations for a sheared suspension at Re=0.01 and 1.0 and ϕ=0.3.

the shear flow is implemented using walls in the gradient direction, with periodicity in the other directions. While this represents experiments better in some measure than a fully periodic model, we are nonetheless limited by this because the results are dependent on position relative to the walls. Hence, it would be useful to compare the results obtained here with those from a LB model with Lees–Edwards boundary conditions.[39]

Newtonian rheology of the suspension, as N_2 undergoes the noted sign change as ϕ increases.

Finally, the probability density functions of transverse velocities were reported. In general, the probability densities undergo a transition from exponential at low ϕ to a Gaussian distribution at relatively higher ϕ. For U_z, however, the Gaussian fit for low velocity fluctuations is accompanied by exponential tails at higher velocities. The role of Reynolds number is to render the velocity distributions narrower in passing from Re=0 to Re=$O(1)$.

We note that the LB method allows simulation of fluid motion with finite inertia, and thus provides a capability not available in Stokesian Dynamics. In the present formulation,

[1]G. K. Batchelor, "The stress system in a suspension of force free particles," J. Fluid Mech. **41**, 545 (1970).

[2]F. A. Gadala-Maria, "The rheology of concentrated suspension," Ph.D. thesis, Stanford University, 1979.

[3]I. E. Zarraga, D. A. Hill, and D. T. Leighton, "The characterization of the total stress of concentrated suspensions of non-colloidal spheres in Newtonian fluids," J. Rheol. **44**, 185 (2000).

[4]A. Singh and P. R. Nott, "Experimental measurements of the normal stresses in sheared Stokesian suspensions," J. Fluid Mech. **490**, 293 (2003).

[5]H. A. Barnes, "Shear-thickening (dilatancy) in suspensions of nonaggregating solid particles dispersed in Newtonian liquids," J. Rheol. **33**, 329 (1989).

[6]J. F. Brady and G. Bossis, "The rheology of concentrated suspensions in simple shear flow by numerical simulations," J. Fluid Mech. **155**, 105 (1985).

[7]J. F. Brady and G. Bossis, "Stokesian dynamics," Annu. Rev. Fluid Mech. **20**, 111 (1988).

[8]A. Sierou and J. F. Brady, "Accelerated Stokesian dynamics simulations," J. Fluid Mech. **448**, 115 (2001).

[9]F. Parsi and F. Gadala-Maria, "Fore-and-aft asymmetry in a concentrated suspension of solid spheres," J. Rheol. **31**, 725 (1987).

[10]J. F. Brady and J. F. Morris, "Microstructure of strongly sheared suspensions and its impact on rheology and diffusion," J. Fluid Mech. **348**, 103 (1997).

[11]D. R. Foss and J. F. Brady, "Structure, diffusion and rheology of Brownian suspensions by Stokesian dynamics simulation," J. Fluid Mech. **407**, 167 (2000).

[12]J. F. Morris and B. Katyal, "Microstructure from simulated Brownian suspension flows at large shear rate," Phys. Fluids **14**, 1920 (2002).

[13]A. Sierou and J. F. Brady, "Rheology and microstructure in concentrated noncolloidal suspensions," J. Rheol. **46**, 1031 (2002).

[14]J. F. Morris and F. Boulay, "Curvilinear flows of noncolloidal suspensions: the role of normal stresses," J. Rheol. **43**, 1213 (1999).

[15]P. R. Nott and J. F. Brady, "Pressure-driven flow of suspensions: simulation and theory," J. Fluid Mech. **275**, 157 (1994).

[16]R. E. Hampton, A. A. Mammoli, A. L. Graham, N. Tetlow, and S. A. Altobelli, "Migration of particles undergoing pressure-driven flow in a circular conduit," J. Rheol. **41**, 621 (1997).

[17]C. J. Lin, J. H. Peery, and W. R. Showalter, "Simple shear flow round a rigid sphere: inertial effects and suspension rheology," J. Fluid Mech. **44**, 1 (1970).

[18]J. Feng, H. H. Hu, and D. D. Joseph, "Direct simulation of initial value problems for the motion of solid bodies in a Newtonian fluid. Part 2. Couette and Poiseuille flows," J. Fluid Mech. **277**, 271 (1994).

[19]P. Y. Huang and D. D. Joseph, "Effects of shear thinning on migration of neutrally-buoyant particles in pressure driven flow of Newtonian and viscoelastic fluid," J. Non-Newtonian Fluid Mech. **90**, 159 (2000).

[20]A. J. C. Ladd, "Numerical simulations of particulate suspensions via a discretized Boltzmann equation. Part 1. Theoretical foundation," J. Fluid Mech. **271**, 285 (1994).

[21]A. J. C. Ladd, "Numerical simulations of particulate suspensions via a discretized Boltzmann equation. Part 2. Numerical results," J. Fluid Mech. **271**, 311 (1994).

[22]C. K. Aidun, Y. Lu, and E. J. Ding, "Direct analysis of particulate suspensions with inertia using the discrete Boltzmann equation," J. Fluid Mech. **373**, 287 (1998).

[23]A. J. C. Ladd and R. Verberg, "Lattice-Boltzmann simulations of particle-fluid suspensions," J. Stat. Phys. **104**, 1191 (2001).

[24]J. Kromkamp, D. T. M. van den Ende, D. Kandhai, R. G. M. van der Sman, and R. M. Boom, "Shear-induced self-diffusion and microstructure in non-Brownian suspensions at non-zero Reynolds number," J. Fluid Mech. **529**, 253 (2005).

[25] Y. Yan, J. F. Morris, and J. Koplik, "Hydrodynamic interaction of two particles in confined linear shear flow at finite Reynolds number," Phys. Fluids **19**, 113305 (2007).

[26] A. Shakib-Manesh, P. Raiskinmäki, A. Koponen, M. Kataja, and J. Timonen, "Shear stress in a Couette flow of liquid-particle suspensions," J. Stat. Phys. **107**, 67 (2002).

[27] P. Raiskinmäki, J. A. Åström, M. Kataja, M. Latva-Kokko, A. Koponen, A. Jäsberg, A. Shakib-Manesh, and J. Timonen, "Clustering and viscosity in a shear flow of a particulate suspension," Phys. Rev. E **68**, 061403 (2003).

[28] J. Hyväluoma, P. Raiskinmäki, A. Kopenen, M. Kataja, and J. Timonen, "Strain-hardening in liquid-particle suspensions," Phys. Rev. E **72**, 061402 (2005).

[29] P. M. Kulkarni and J. F. Morris, "Pair-sphere trajectories in finite Reynolds number shear flow," J. Fluid Mech. **596**, 413 (2008).

[30] G. K. Batchelor and J. T. Green, "The hydrodynamic interaction of two small freely-moving spheres in a linear flow field," J. Fluid Mech. **56**, 375 (1972).

[31] N. Q. Nguyen and A. J. C. Ladd, "Lubrication corrections for lattice-Boltzmann simulation of particle suspensions," Phys. Rev. E **66**, 046708 (2002).

[32] S. Kim and S. J. Karrila, *Microhydrodynamics: Principles and Selected Applications* (Butterworth-Heinemann, Boston, MA, 1991).

[33] D. R. Mikulencak and J. F. Morris, "Stationary shear flow around fixed and free bodies at finite Reynolds number," J. Fluid Mech. **520**, 215 (2004).

[34] C. A. Kossack and A. Acrivos, "Steady simple shear flow past a circular cylinder at moderate Reynolds number: a numerical solution," J. Fluid Mech. **66**, 353 (1974).

[35] G. Subramanian and D. L. Koch, "Inertial effects on the transfer of heat or mass from neutrally buoyant spheres in a steady linear velocity field," Phys. Fluids **18**, 073302 (2006).

[36] D. T. Leighton, "The shear induced migration of particulates in concentrated suspensions," Ph.D. thesis, Stanford University, 1985.

[37] G. K. Batchelor and J. T. Green, "The determination of the bulk stress in a suspension of spherical particles to order c^2," J. Fluid Mech. **56**, 401 (1972).

[38] G. Drazer, J. Koplik, B. Khusid, and A. Acrivos, "Deterministic and stochastic behavior of non-Brownian spheres in sheared suspensions," J. Fluid Mech. **460**, 307 (2002).

[39] A. J. Wagner and I. Pagonabarraga, "Lees–Edwards boundary conditions for lattice Boltzmann," J. Stat. Phys. **107**, 521 (2002).